Separation of parallel encoded complex-valued slices (SPECS) from a single complex-valued aliased coil image

Daniel B. Rowe [a,b,*], Iain P. Bruce [c], Andrew S. Nencka [b], James S. Hyde [b], Mary C. Kociuba [a]

[a] Department of Mathematics, Statistics, and Computer Science, Marquette University, Milwaukee WI, USA
[b] Department of Biophysics, Medical College of Wisconsin, Milwaukee WI, USA
[c] Duke/UNC Brain Imaging and Analysis Center, Duke University, Durham, NC, USA

ARTICLE INFO

ABSTRACT

Purpose: Achieving a reduction in scan time with minimal inter-slice signal leakage is one of the significant obstacles in parallel MR imaging. In fMRI, multiband-imaging techniques accelerate data acquisition by simultaneously magnetizing the spatial frequency spectrum of multiple slices. The SPECS model eliminates the consequential inter-slice signal leakage from the slice unaliasing, while maintaining an optimal reduction in scan time and activation statistics in fMRI studies.
Materials and methods: When the combined *k*-space array is inverse Fourier reconstructed, the resulting aliased image is separated into the un-aliased slices through a least squares estimator. Without the additional spatial information from a phased array of receiver coils, slice separation in SPECS is accomplished with acquired aliased images in shifted FOV aliasing pattern, and a bootstrapping approach of incorporating reference calibration images in an orthogonal Hadamard pattern.
Result: The aliased slices are effectively separated with minimal expense to the spatial and temporal resolution. Functional activation is observed in the motor cortex, as the number of aliased slices is increased, in a bilateral finger tapping fMRI experiment.
Conclusion: The SPECS model incorporates calibration reference images together with coefficients of orthogonal polynomials into an un-aliasing estimator to achieve separated images, with virtually no residual artifacts and functional activation detection in separated images.

© 2015 Elsevier Inc. All rights reserved.

1. Introduction

In functional MRI (fMRI), fluctuations in the BOLD signal are observed in different regions of the brain through a discrete time series of images. Traditionally, each slice of the volume is excited individually, with enough data to reconstruct an image for that slice measured in a single *k*-space readout. To improve the temporal resolution of fMRI data, parallel MRI (pMRI) models [1–3] perform an in-plane acceleration within each slice by omitting rows of the spatial frequency measurements. As these methods offer a reduction in scan time, this process is still time consuming; it is possible to simultaneously magnetize multiple slices at once, measuring sufficient data in a single *k*-space readout to be reconstructed into a single aliased image that represents a combination of the slices. When acquired with multiple coils, such an aliased image can be separated using coil sensitivity profiles for spatial localization, but the method outlined in this manuscript enables separation of a single aliased image acquired by a quadrature coil into multiple complex-valued fully acquired images.

Significant interest has grown in the simultaneous acquisition of multiple slices in a volume through simultaneous multi-slice (SMS) imaging techniques. Initial SMS studies presented a means of separating two slices that were simultaneously acquired by a single coil [4,5]; these studies were later extended to separate multiple slices simultaneously acquired by multiple coils [6–14]. At high acceleration factors, coil sensitivities do not have sufficient information to determine in which of the un-aliased voxels a BOLD signal increase occurred, and thus inter-slice signal leakage could spread the activation to the previously aliased voxels. Efforts have been made to characterize and alleviate inter-slice signal leakage in separated slices in the context of multi-coil SMS models [15–17]. With a single channel quadrature coil, magnitude-only models for separating simultaneously encoded slices have been investigated, although these models are constrained to only separating two slices [14,18–21]. These magnitude-only SMS reconstruction techniques are conceptually similar to phase constrained in-plane acceleration methods [22,23], but it has been well documented that the judicious use of appropriately characterized magnetization phase can vastly improve the un-aliasing process in parallel imaging [22–24].

Additionally, a recent line of research has illustrated that utilizing images in a time series with both magnitude and phase offers improved fMRI activation statistics [25–28] over those achieved through the gold standard magnitude-only models.

The un-aliasing technique outlined in this manuscript performs a Separation of Parallel Encoded Complex-valued Slices (SPECS) simultaneously excited by a single channel quadrature coil [29]. The SPECS model first addresses the inter-slice signal leakage in fMRI data by simultaneously separating multiple acquisitions of aliased slices in which the phase of the various slices is systematically shifted as done with the blipped-CAIPI model [30]. With a single channel quadrature coil model, implementing a shifted FOV in the aliased time-series acquisition scheme improves slice separation from the greater variability among signal in the aliased voxels. Secondly, the SPECS reconstruction technique reduces inter-slice signal leakage from the un-aliasing process by incorporating boot-strap-sampled calibration images in the time-series separation algorithm. The shifted FOV acquisition with the SPECS reconstruction allows for multiple acquisitions with unique aliasing patterns, and for the separation of more than two simultaneously encoded slices acquired with a single quadrature coil. The SPECS approach increases the rate of observing brain function, while minimizing inter-slice signal leakage and placing functional activation in fMRI data.

2. Theory

To outline the SPECS model, the orthogonal separating matrix is presented for a single aliasing pattern in which no shift has been applied during acquisition. The model is then expanded to simultaneously separate multiple slices with unique phase shifts, such that various aliasing patterns exist for each voxel. The statistical reasoning behind the mechanism of reducing inter-slice signal leakage in SPECS through incorporating a bootstrap mean calibration image is also presented.

2.1. Image aliasing

For an acceleration factor of $A = N_S$, N_S slices are acquired simultaneously in a single aliased image using a single coil. Consider a single voxel in the same spatial location across N_S slices. The voxel value in the zth slice is complex-valued, and the true noiseless voxel value is denoted by $y_z = \beta_{Rz} + i\beta_{Iz}$, where β_{Rz} and β_{Iz} are the true real and imaginary components. Each complex-valued aliased voxel, is described as the sum of the real and imaginary components with added complex-valued measurement error,

$$\begin{pmatrix} a_R \\ a_I \end{pmatrix} = \begin{pmatrix} 1,...,1 & 0 \\ 0 & 1,...,1 \end{pmatrix} \left(\beta_{R1},...,\beta_{RN_S}, \beta_{I1},...,\beta_{IN_S} \right)^T + \begin{pmatrix} \varepsilon_R \\ \varepsilon_I \end{pmatrix}. (1)$$

Eq. (1) may also be written as $a = (I_2 \otimes X_A)\beta + \varepsilon$, where a is 2×1 vector representing the observed real and imaginary aliased image voxel values, I_2 is the 2×2 identity matrix, X_A is a $1 \times N_S$ vector of ones, and β is a $2N_S \times 1$ vector representing the real and imaginary true fully acquired voxel values for the N_S images. The measurement error, ε, is a 2×1 vector with a zero mean, $E(\varepsilon_R, \varepsilon_I)^T = 0$, and a covariance of $cov(\varepsilon_R, \varepsilon_I)^T = \sigma^2 I_2$.

To separate the N_S aliased slices, a least squares estimation results in a solution of the form $\hat{\beta} = (I_2 \otimes X_A^{-1})a$. However, since the aliasing matrix in Eq. (1), $(I_2 \otimes X_A)$, represents a system of two equations with $2N_S$ unknowns, it is neither square nor invertible, and thus a unique solution for β cannot generally be found. One proposed solution [11,14] is the pseudo-inverse [31], which provides a unique solution in the least squares sense, but not necessarily the correct solution. In this manuscript, we present a novel means of improving the rank of the design matrix in Eq. (1) by incorporating orthogonal polynomials

with X_A, such that the resulting system of equations is invertible and can be used to separate two or more aliased slices acquired with a single coil.

2.2. Artificial aliasing of the calibration reference images

As with all pMRI and SMS reconstruction models, the separation of aliased voxels is performed using additional calibration measurements. In most pMRI studies, additional localized spatial information is drawn from these measurements to determine coil sensitivity profiles. For a least squares separation in these models, the number of coils must exceed the number of aliased voxels to achieve a full rank unaliasing matrix. In SPECS, this constraint is relaxed with a single channel quadrature coil, since the additionally acquired calibration measurements are used for both spatial localization in the separation process and improving the rank of X_A.

Consider a time series of length m fully sampled calibration images for the N_S slices. At time point t, a single voxel in slice z of the calibration images is denoted by $\nu_{zt} = (\mu_{Rz} + i\mu_{Iz}) + (\eta_{Rz,t} + i\eta_{Iz,t})$, where μ_{Rz} and $\mu_{Iz,}$ are the true real and imaginary components, while $\eta_{Rz,t}$ and $\eta_{Iz,t}$ denote the real and imaginary components of the measurement error, with a mean of $E(\eta_{Rt}^T, \eta_{It}^T)^T = 0$ and a covariance of $cov(\eta_{Rt}^T, \eta_{It}^T)^T = \sigma^2 I_{NS}$. The mean of the m calibration images for a voxel values in the same location across N_S slices is written into a sum of two real-valued vectors,

$$\bar{\nu} = \begin{pmatrix} \bar{\nu}_R \\ \bar{\nu}_I \end{pmatrix} = \left(\bar{\nu}_{R,1},...,\bar{\nu}_{R,N_S}, \bar{\nu}_{I1},...,\bar{\nu}_{I,N_S} \right)^T, \qquad (2)$$

where $\bar{\nu}_R$ and $\bar{\nu}_I$ denote $N_S \times 1$ vectors with the mean real and imaginary component of the N_S voxel values. The mean calibration vector, $\bar{\nu}$, is incorporated into the SPECS model with an artificial Hadamard aliasing scheme.

The aliasing process outlined in Eq. (1) represents an under-determined system of two equations and $2N_S$ unknowns. To make the aliasing matrix, $(I_2 \otimes X_A)$, in Eq. (1) square and invertible, $(N_S - 1)$ rows are added to both X_A and a. The SPECS approach constructs an $(N_S - 1) \times N_S$ artificial aliasing matrix, C, in a Hadamard pattern. The artificial aliasing matrix, C, represents $(N_S - 1)$ orthogonal ways the true voxel values in the N_S slices could be aliased, and is combined with X_A to form a new aliasing matrix $(I_2 \otimes [X_A^T, C^T]^T)$. The vector a, in Eq. (1), is converted from the 2×1 vector of observed aliased voxel values to a $2N_S \times 1$ vector, y. Now, both observed aliased voxel values and artificially aliased voxel values drawn from the mean calibration vector, $\bar{\nu}$, in Eq. (2) are represented by

$$y = \begin{pmatrix} a_R \\ C\bar{\nu}_R \\ a_I \\ C\bar{\nu}_I \end{pmatrix} = \begin{pmatrix} X_A\beta_R \\ C\mu_R \\ X_A\beta_I \\ C\mu_I \end{pmatrix} + \begin{pmatrix} \varepsilon_R \\ C\eta_R \\ \varepsilon_I \\ C\eta_I \end{pmatrix}. \qquad (3)$$

In Eq. (3), the added error vector is the measurement error of the observed aliased voxels, $\varepsilon = (\varepsilon_R, \varepsilon_I)^T$, and the artificially aliased mean calibration images, $\eta = (C\eta_R^T, C\eta_I^T)^T$. However, since the artificially aliased voxels, $C\bar{\nu}_R$ and $C\bar{\nu}_I$, in the vector y are obtained from mean calibration images, the terms $C\eta_R$ and $C\eta_I$ in Eq. (3) are replaced by $(N_S - 1) \times 1$ vectors of zeros.

2.3. Complex-valued image separation model

Since the matrix $X = [X_A^T, C^T]^T$ is orthogonal and full rank, the complex-valued images of the N_S aliased slices can be separated by the least squares estimate $\hat{\beta} = (X^TX)^{-1}X^Ty$, or

$$\hat{\beta} = \left[I_2 \otimes \left(X_A^T X_A + C^T C \right)^{-1} \left(X_A^T, C^T \right) \right] y. \qquad (4)$$
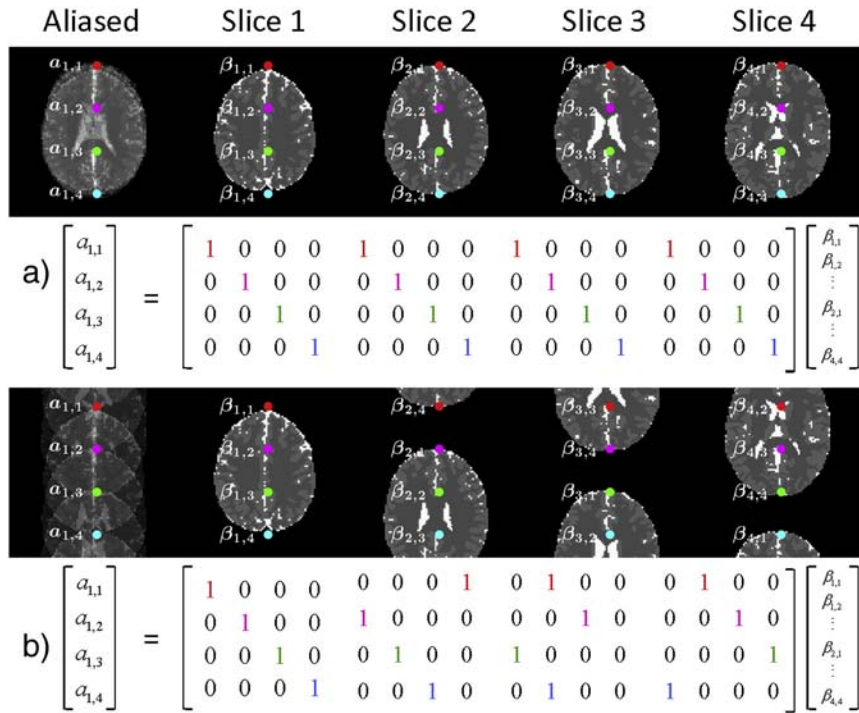
Fig. 1. Aliasing $N_S = 4$ slices (a) without applying any FOV shift, and (b) applying a FOV shift of $(j - 1)$FOV/N_S to slice $j = [1,..,N_S = 4]$ prior to aliasing.

Note, the term $C^T C$ acts as a regularizer for a matrix inverse, and the expected value of the least squares estimate is derived in Appendix A. Alternatively one can view this as a Bayesian procedure where the separated images are a weighted combination of prior and likelihood means.

The covariance of the measurement error in Eq. (1), $\text{cov}(\varepsilon_R, \varepsilon_I)^T = \sigma^2 I_2$, assumes no covariance between a_R and a_I with a constant variance of σ^2 for both a_R and a_I. If the same artificially aliased calibration voxels, $C\bar{v}_R$ and $C\bar{v}_I$, are used to separate each aliased image in the time-series, then there is no variability and the covariance of the measurements in the vector y is of the form

$$\Gamma = \text{cov}(y) = I_2 \otimes \begin{bmatrix} \sigma^2 & 0 & \cdots & 0 \\ 0 & \tau^2 & \cdots & 0 \\ \vdots & \vdots & \ddots & \vdots \\ 0 & 0 & \cdots & \tau^2 \end{bmatrix} \tag{5}$$

where $\tau^2 = 0$. When the estimator in Eq. (4) is calculated using Eq. (5) with $\tau^2 = 0$, the covariance of $\hat{\beta}$ is

$$\text{cov}(\hat{\beta}) = (X^{-1}) \Gamma (X^{-1})^T = \frac{\sigma^2}{N_S^2}(I_2 \otimes J_{N_S}). \tag{6}$$

where J_{NS} is a $N_S \times N_S$ matrix of ones [32]. When the covariance structure in Eq. (6) is converted to a correlation matrix, it becomes

$$\text{corr}(\hat{\beta}) = I_2 \otimes J_{N_S}. \tag{7}$$

The result in Eq. (7) indicates that the real and imaginary values in $\hat{\beta}$ are perfectly correlated with themselves, and there is no correlation between the real and imaginary values in $\hat{\beta}$.

The artificial correlation induced in $\hat{\beta}$ with Eq. (7) can be eliminated through a bootstrapping adaptation. So if N_S calibration images are aliased with the artificial aliasing matrix, C, then the artificially aliased measurements will have a variance of σ^2, rather than 0, scaled by the sum of squares of the rows in C, as described in Appendix B. If an $N_S \times N_S$ Hadamard coefficient matrix is chosen for X, where the matrix C is comprised of the lower $N_S - 1$ rows of X, then the sum of squares for each row in C will be N_S. For a bootstrapping approach with Hadamard coefficients, one can therefore average N_S randomly selected calibration images in $\bar{v}$ to obtain $\tau^2 = \sigma^2$, such that the covariance in Eq. (5) becomes

$$\Gamma = \text{cov}(y_C) = \sigma^2 I_{2N_S}. \tag{8}$$

As the covariance of the SPECS model with a bootstrapping approach in Eq. (8) is strictly diagonal, the correlation structure induced in $\hat{\beta}$ becomes an identity matrix. Thus, no correlation is induced from the separation process, and inter-slice signal leakage is minimized.

3. Methods and materials

To illustrate an application of the SPECS model, a simulation was performed in which $N_z = 8$ slices of size 96×96 of a human brain phantom and experimental data, were aliased together with a single quadrature coil (assuming a homogeneous B_1-field).

For a data set with no acceleration, $A = 1$, a single un-shifted acquisition of each slice was simulated. For $A = 2$, the $N_z = 8$ slices are acquired in $N_p = 2$ packets each containing $N_s = 4$ slices in $N_{acq} = 2$ acquisitions. For $A = 4$ the $N_z = 8$ slices are acquired in $N_p = 1$ packet containing $N_s = 8$ slices in $N_{acq} = 2$ acquisitions. The term packets refers to the number of aliased slice groups, i.e. $N_p = 2$ and $N_z = 8$ correspond to two packets with four slices in each packet. The details of incorporating multiple acquisitions with unique FOV shifting patterns in the SPECS model are described in Appendix B. For acquisitions $acq = 1,...,N_{acq}$, slices $j = 1,..., N_s$ were shifted by $(acq - 1)(j - 1)\Delta$ in the PE dimension, where $\Delta = 96/N_s$ voxels. This scheme places no FOV shift on the first acquisition while the remaining $N_{acq} - 1$ acquisitions are subject to different shifting schemes similar to those presented in Fig. 1.
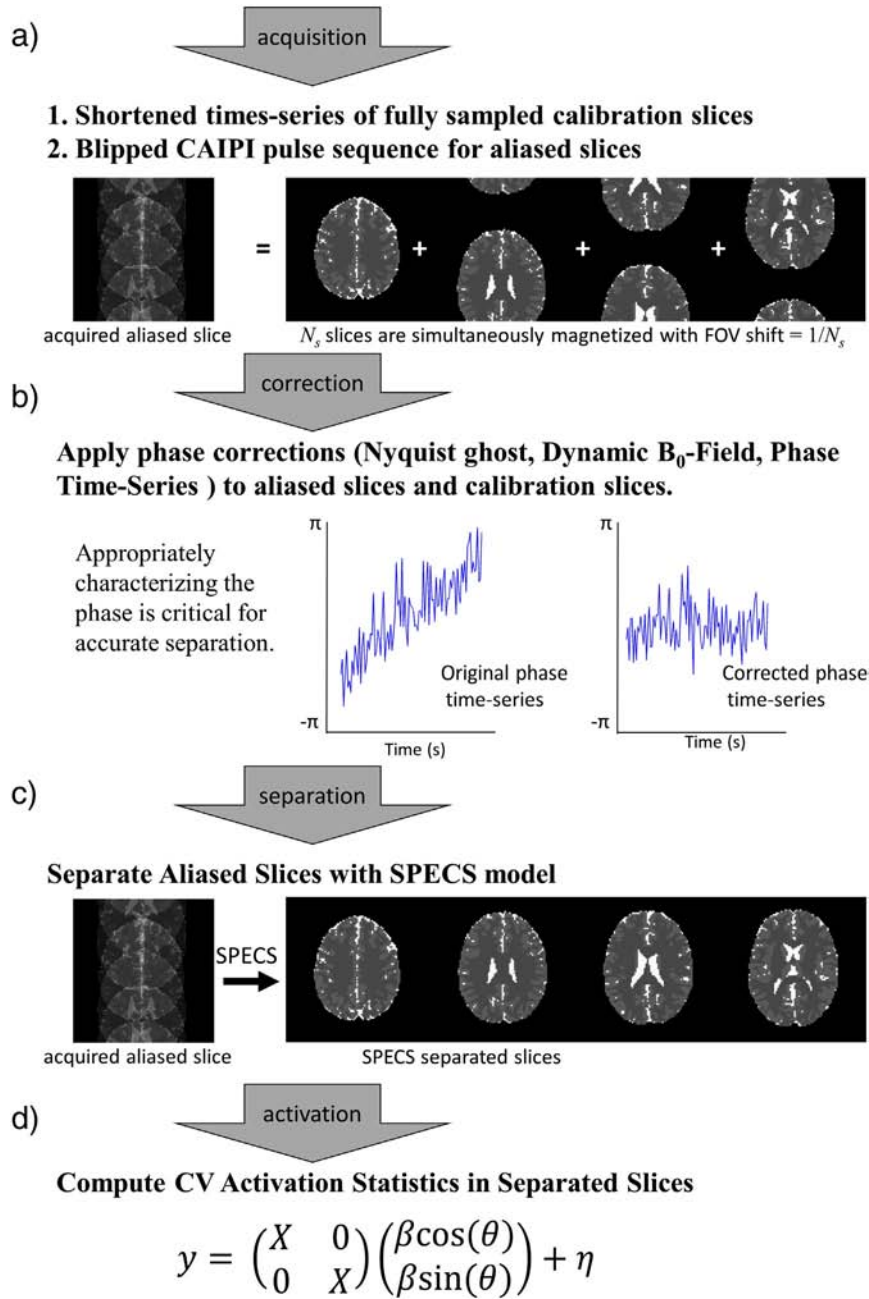
Fig. 2. A diagram outlining the data acquisition and processing pipeline to implement the SPECS model in four main steps.

3.1. Phantom data example

A simulated fMRI phantom data set was generated with task in a block design with an initial 16 s rest followed by 22 epochs of 16 s on and 16 s off using MATLAB (The Mathworks, Natick, MA, USA) to mimic a single channel quadrature head coil. The data were generated with eight axial slices that are 96×96 in dimension. A noiseless time series was generated for each slice with a theoretical T_2^* weighted phantom similar to [33]. The initial T_2^* weighted phantom has values between 0 and 1, and was generated with the echo time (TE) and effective echo spacing (EESP) used during the acquisition of the experimental data. A signal-to-noise ratio (SNR) of 13 and contrast-to-noise ratio (CNR) of 0.25 values were used for this simulation, which were also based upon the experimental human data. The magnitude of the phantom was scaled to 13 in the

grey matter, and the phase in each slice was set to a constant value within the brain phantom that varied from zero to π from slice eight to slice one.

A block-design of task activity was simulated in one unique 4×4 voxel square region of interest (ROI) rotating clockwise for each of slice. The magnitude within the ROI is increased by 0.25 for 16 TRs and then returns to baseline for the following 16 TRs. A main goal of the SPECS model is faster observation of brain function; to illustrate this mechanism time-series of 180, 360, and 720 time repetitions (TRs) are generated for the accelerations, $A = 1$, $A = 2$, and $A = 4$, respectively. A time series of 16 calibration images, with no simulated task, was generated for each slice. For each of the N_{acq} acquisitions, the true noiseless time series of each slice was appropriately shifted in the PE dimension before the slices were all aliased together. Standard Gaussian noise was added to the real and
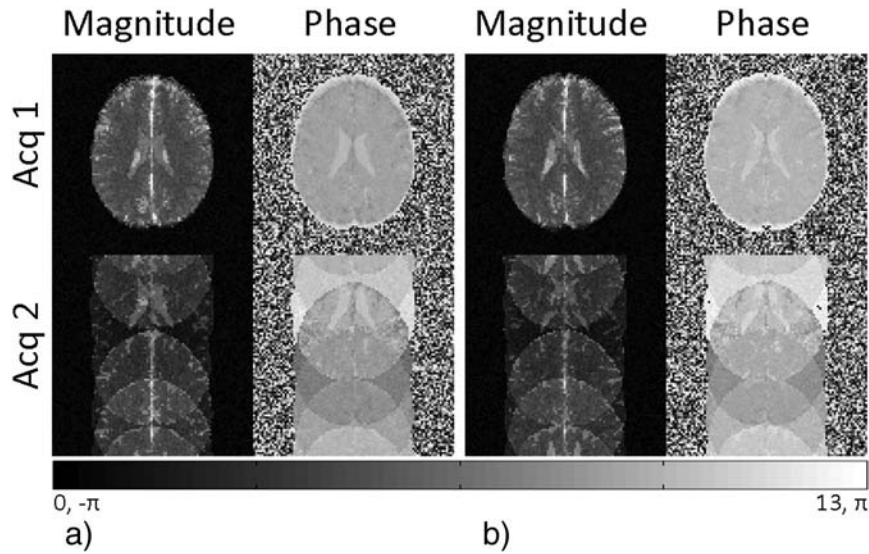
Fig. 3. Aliased phantom acquisitions for $A = 2$; the $N_z = 8$ slices are acquired in $N_p = 2$ packets, (a) the magnitude and phase for packet 1, and (b) the magnitude and phase for packet 2, each containing $N_s = 4$ slices in $N_{acq} = 2$ acquisitions.

imaginary parts of each TR of the aliased images and the calibration images. The aliased images were then separated using the SPECS model with Hadamard coefficients for the matrix C in Eqs. (4) and (B.1). The separated images were smoothed with a full-width-at-half-max (FWHM) of two voxels. Finally, fMRI activation was calculated in each separated voxel using the complex-valued fMRI model in [25].

3.2. Experimental data example

An experimental fMRI human data set was acquired with bilateral finger tapping in a block design with an initial 16 s rest followed by 22 epochs of 16 s on and 16 s off using a 3.0 T Discovery MR750 MRI scanner (General Electric, Milwaukee, WI) with a GE single channel quadrature head coil. The data were acquired with ten interleaved axial slices that are 96×96 in dimension and 4 mm thick. The two most inferior slices were omitted so that there were eight utilized. The imaging parameters included a 24.0 cm FOV, a TR/TE of 1000/39 ms, a flip angle of 25°, an acquisition bandwidth of 111 kHz, and an effective echo spacing of 0.672 ms. The phase encoding direction was oriented as posterior to anterior (bottom to top in images). In image reconstruction, images were Nyquist ghost corrected using the three navigator echoes method [34] and dynamic B0 field corrected using the TOAST single echo technique [33,35]. The phase images were further corrected by subtracting a local second order polynomial fit to their difference from the mean. The acquisition and processing pipeline for experimental data is described in Fig. 8.

Over the course of 22 epochs, bilateral finger tapping was performed in a block-design to elicit functional activation in the sensorimotor area. It was found that the SNR in activated regions was about 13 and CNR was about 0.25, which were utilized for the previous simulation. For each of the N_{acq} acquisitions, the measured time series of each slice was appropriately shifted in the PE dimension before the slices were all aliased together. A main goal of the SPECS model is faster observation of brain function, to illustrate this mechanism time-series of 180, 360, and 720 TRs are used for the accelerations, $A = 1$, $A = 2$, and $A = 4$, respectively. The first 16 images of the time series, when no task is performed, were used as the calibration images. The aliased images were then separated using the SPECS model with Hadamard coefficients for the matrix C in Eq. (4) and (B.1). The separated images were smoothed

with a FWHM of two voxels. Finally, fMRI activation was calculated in each separated voxel using the complex-valued fMRI model in [25]. The data acquisition and processing pipeline to implement the SPECS model is outlined in the diagram in Fig. 2.

4. Results

4.1. Phantom data example

In Fig. 3, the images for the first aliased TR to be separated are presented when $A = 2$. In Fig. 3(a) are the magnitude and phase as columns for the first acquisition in the first row and the second acquisition in the second row for packet 1. In Fig. 3(b) are the magnitude and phase as columns for the first acquisition in the first row and the second acquisition in the second row for packet 2. The magnitude and phase of the separated images for the calibration images ($A = 1$) and $A = 2$ and 4 are presented in Fig. 4. In Fig. 4(a) the fully measured averaged calibration images are presented for all 8 slices that are used to separate the first TR of aliased images. In Fig. 4(b) and (c) are all 8 of the separated magnitude and phase slices for the first TR in the aliased time series which were separated from the $N_{acq} = 2$ and $N_{acq} = 1$ aliased magnitude and phase images in Fig. 3 by inserting Eq. (B.1) into Eq. (4). The slices that are initially aliased into packet 1 and packet 2 are distinguished in Fig. 4(b) with the white numbering scheme. There are no signs of residual aliasing artifacts in any of the separated images. The incorporation of artificially aliased calibration images makes the system of equations in Eq. (3) over-determined, allowing such accelerations in data acquired with a single coil.

After slice separation, fMRI activation was calculated in each voxel of all separated slices using the complex-valued model in [25]. The z-scores denoting activation statistics are presented in Fig. 5 with the ROIs containing truly active voxels highlighted by pink squares in each slice. The activation maps were thresholded at a z value of 3.5, and the noise outside the phantom was masked. The white numbering for each slice in Fig. 5 corresponds to the packet numbers for each acceleration. Any cluster of "active" voxels that are outside of these squares denotes false positives resulting either from the added noise or from residual effects of aliasing. In Fig. 5(a) are the activation maps for an acceleration factor of $A = 1$, in Fig. 5(b) are the activation maps for an acceleration factor of $A = 2$, while in Fig. 5(c) are the activation
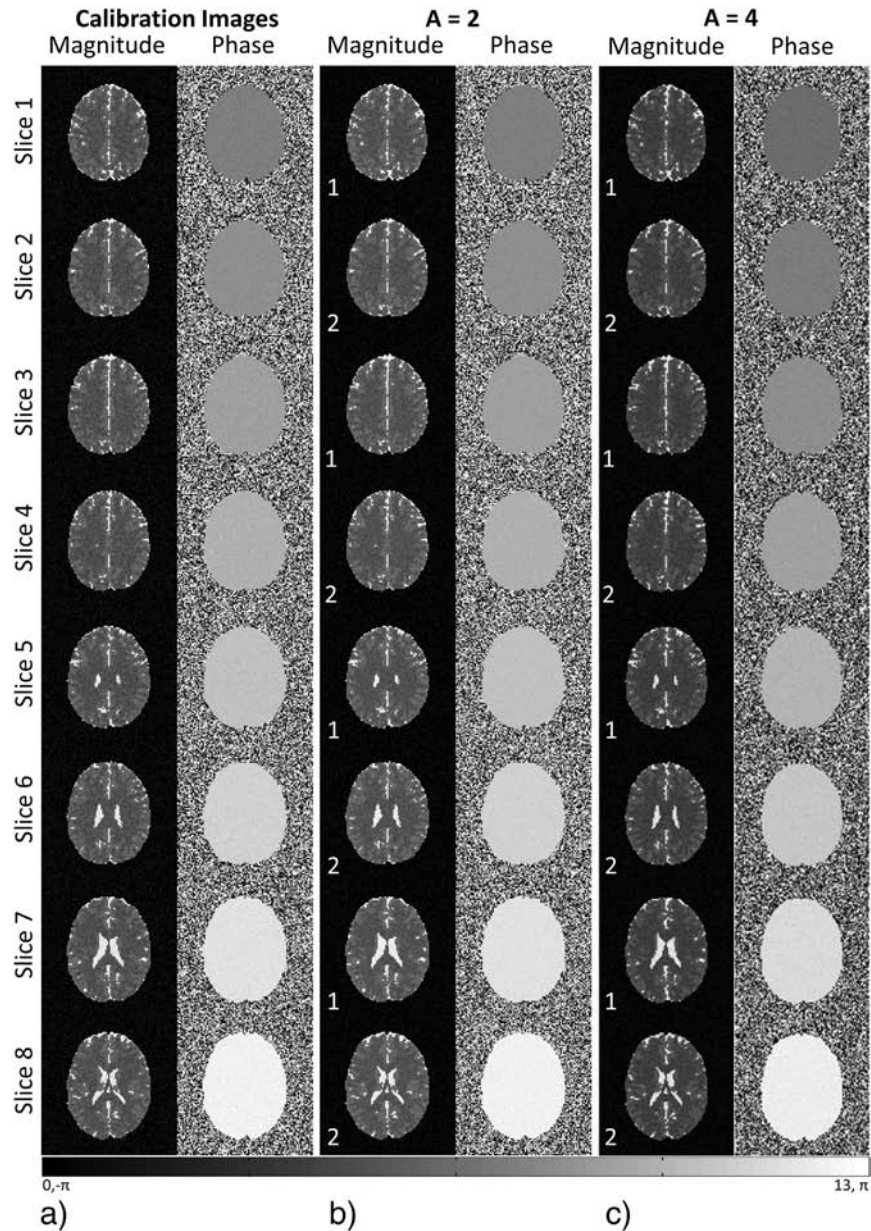
Fig. 4. For the first TR, the SPECS model separates the magnitude and phase images acquired by a single coil, as shown in Fig. 3, (a) with the mean of randomly selecting calibration slices into eight magnitude and phase images with no visual residual aliasing artifacts for (b) $A = 2$, and (c) $A = 4$. The white numbering scheme in (b) and (c) corresponds to the packet the slice was initially aliased into.

maps for an acceleration factor of $A = 4$. The activation statistics in Fig. 5 show strong clusters of activation within the truly active ROIs. This is because the upper $N_S N_{acq}$ equations of the aliasing matrix in Eq. (B.1) represent the aliasing structure of the acquired aliased voxel values, in which the increase in BOLD signal strength is recorded. The activation statistics also increase as acceleration increases, since a higher sampling rate corresponds to a larger sample size and strengthened statistical significance.

As such, the undetermined system of 16 equations (in the case of $A = 4$ with $N_{acq} = 2$ acquisitions) and 8^2 unknowns is able to separate most of the activation statistics in the separating process, but not all of them. In Fig. 5(c), one can observe some minor areas of false activation in the $A = 4$ case. The separation of activation is improved when $N_{acq} = 2$ acquisitions are obtained in the case of $A = 2$, where one can see that the additional clusters of false positives are reduced compared to the case of $A = 4$. With the

exception of only a few clusters of false positives in $A = 2$, the activation statistics for all 8 slices closely resemble the true structure noted when no acceleration is performed with $A = 1$.

4.2. Experimental data example

In Fig. 6, the images for the first aliased TR to be separated are presented when $A = 2$. In Fig. 6(a) are the magnitude and phase as columns for the first acquisition in the first row and the second acquisition in the second row for packet 1. In Fig. 6(b) are the magnitude and phase as columns for the first acquisition in the first row and the second acquisition in the second row for packet 2. The magnitude and phase of the separated images for the calibration images ($A = 1$) and $A = 2$ and 4 are presented in Fig. 7. In Fig. 7(a) the fully measured averaged calibration images are presented for all 8 slices that are used to separate the first TR of aliased images. In
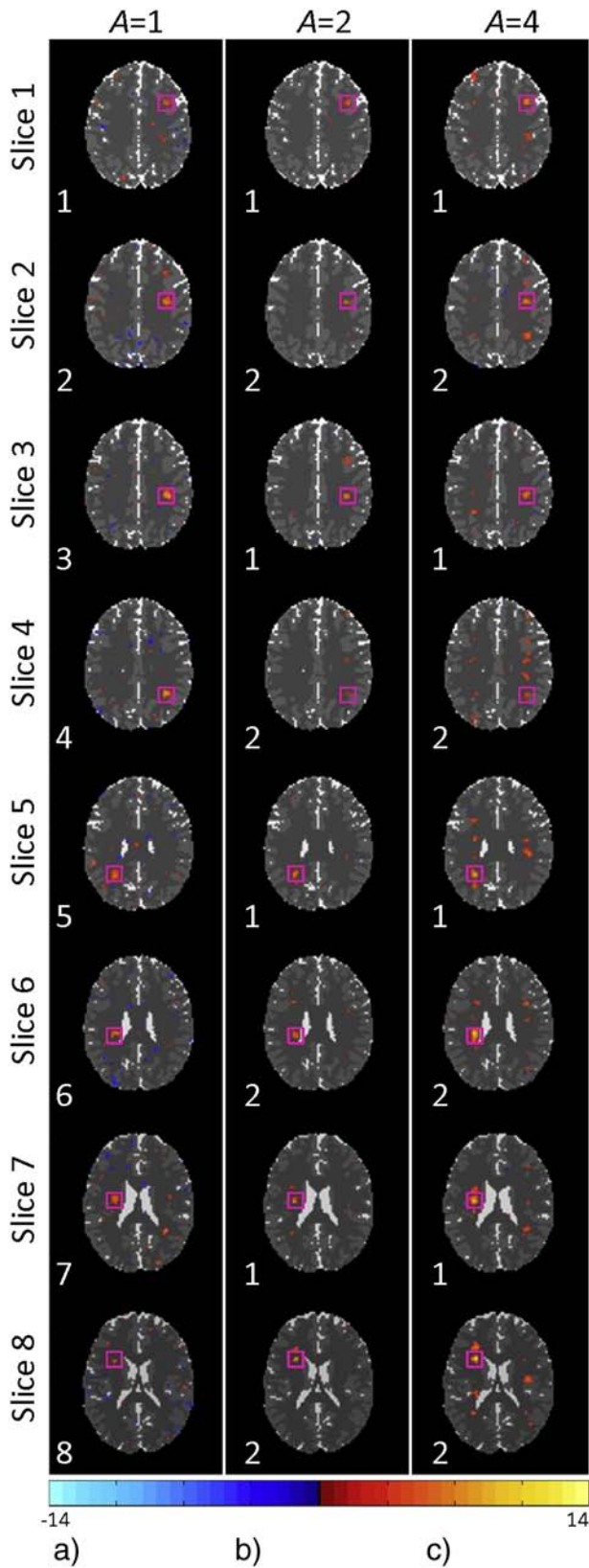
Fig. 5. With the phantom simulation, fMRI activation statistics estimated with a complex-valued model in each voxel of each slice after separating 8 aliased slices with the SPECS model. Activation statistics are presented for data reconstructed from (a) eight acquisitions and eight packets, $A = 1$, (b) two acquisitions and two packets, $A = 2$, and (c) two acquisitions and one packet, $A = 4$. Pink squares indicate regions of true functional activity in slices. The white numbering scheme corresponds to the packet the slice was initially aliased into.

Fig. 7(b) and (c) are all 8 of the separated magnitude and phase slices for the first TR in the aliased time series which were separated from the $N_{acq} = 2$ and $N_{acq} = 1$ aliased magnitude and phase images in Fig. 6 by inserting Eq. (B.1) into Eq. (4). The slices that are initially aliased into packet 1 and packet 2 are distinguished in Fig. 7(b) with the white numbering scheme. As with the phantom simulation, there are no signs of residual aliasing artifacts in any of the separated images. The incorporation of artificially aliased calibration images makes the system of equations in Eq. (3) over-determined, allowing such accelerations in data acquired with a single coil.

After slice separation, fMRI activation was calculated in each voxel of all separated slices using the complex-valued model in [25]. The z-scores denoting activation statistics are presented in Fig. 8 with expected activation being in the sensorimotor area of slices. All activation maps were thresholded at a z value of 3.2, and the noise outside the brain was masked. The white numbering for each slice in Fig. 8 corresponds to the packet numbers for each acceleration. Since adjacent slices were always in different packets, we can see the true activation which did not originate from the separation process. The data have been minimally processed to prevent induced correlations, thus there are motion artifacts around the edges of the brain and within the CSF apparent in the activation maps. In Fig. 8(a) are the activation maps for an acceleration factor of $A = 1$, in Fig. 8(b) are the activation maps for an acceleration factor of $A = 2$, while in Fig. 8(c) are the activation maps for an acceleration factor of $A = 4$. The activation statistics in Fig. 8 show strong clusters of activation within the truly active regions of interest. This is because the upper $N_S N_{acq}$ equations of the aliasing matrix in Eq. (B.1) represent the aliasing structure of the acquired aliased voxel values, in which the increase in BOLD signal strength is recorded. As in the phantom simulation, activation statistics also increase as acceleration increases, since a higher sampling rate corresponds to a larger sample size and strengthened statistical significance.

In the $A = 1$, when no acceleration is performed, activation is observed in the motor cortex most notably in slice 2, and also seen in slice 1 and slice 3. Additional "active" voxels that are outside of these slices, not observed in the $A = 1$ case, denote false positives resulting either from the added noise or from residual effects of aliasing. With increased acceleration, the activation statistics in Fig. 8 show activation within the motor cortex and several additional clusters of "active" voxels within inferior slices to the motor cortex. In Fig. 8(a), the activation statistics are presented for all 8 slices when no acceleration is performed with $A = 1$. The separation of activation is reduced when $N_{acq} = 2$ acquisitions are obtained in the case of $A = 2$. Although, not as significant as observed in the phantom data, there is an increase of activation and regions of activation, in comparison of $A = 2$ in Fig. 8(b) to $A = 4$ in Fig. 8(c). Despite the increased activation from $A = 2$ in Fig. 8(b) to $A = 4$ in Fig. 8(c), there is also more residual noise outside the motor cortex in $A = 4$.

5. Discussion

As the 3-dimensional array of spatial frequencies used to generate each volume of images in the time series is not acquired instantaneously, acquisition schemes often place constraints on both the spatial and temporal resolution of the acquired data. There is a lack of techniques offering a true time reduction in data acquisition while preserving the BOLD signal, for faster observation of brain function in fMRI studies. When fMRI data are acquired with multi-coil parallel MRI models, the number of coils is typically required to greatly exceed the acceleration factor by which the data are sampled in order for the inverse problem to be solved. In these models the calibration data accurately separate the structural images; it is challenging to separate functional activity in the aliased images.
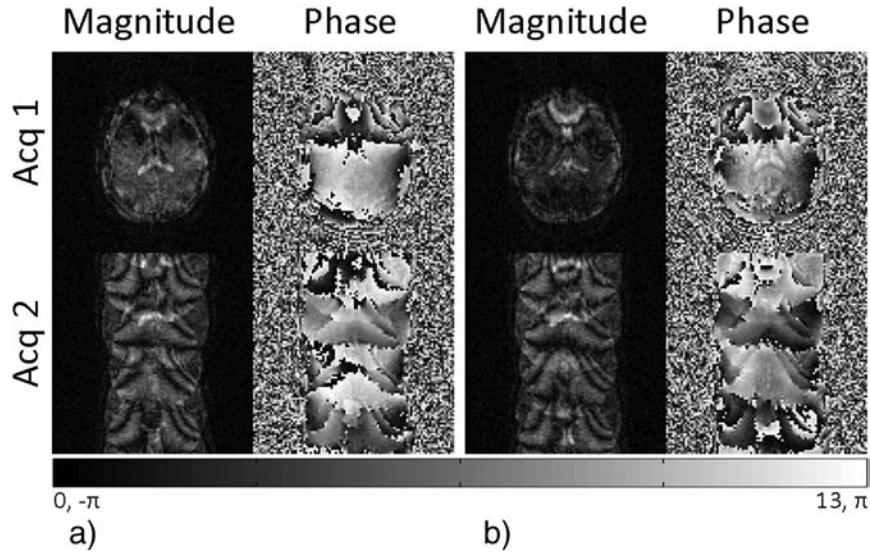
Fig. 6. Aliased experimental data acquisitions for $A = 2$; the $N_z = 8$ slices Magn Reson Imagingare acquired in $N_p = 2$ packets, (a) the magnitude and phase for packet 1, and (b) the magnitude and phase for packet 2, each containing $N_s = 4$ slices in $N_{acq} = 2$ acquisitions.

Acquiring various acquisitions of the same aliased slices in which the different slices are shifted in the PE dimension, allows multiple ways in which each voxel in a slice can be aliased with other voxels of other slices. The use of multiple acquisitions in the SPECS model therefore enables one to achieve realistic accelerations in data acquisition by factors of up to $A = 4$, while simultaneously improving the power of determining in which of the aliased slices an increase in the BOLD signal amplitude originated. Although, inter-slice signal leakage is visible in the reconstructed images in $A = 4$, and for a single quadrature coil acquisition an acceleration of $A = 2$ is recommended for the SPECS model. The model reduces inter-slice signal leakage through eliminating correlation between separated slices with the bootstrap sampling to uniquely unalias each TR. As observed in Fig. 8(c), a potential weakness of the model is the aliasing artifacts present in separated slice images for $A = 4$. While the phantom simulation only had slight inter-slice signal leakage corresponding to activation locations from other slices, the experimental data had motion artifacts across the separated slices. The motor cortex was easily distinguishable despite the artifacts with the increased acceleration. However, to achieve a higher acceleration, incorporating a rigorous motion correction operation in the processing pipeline would be essential to detect activation. The SPECS model outlined in this manuscript presents a novel means of incorporating calibration images artificially aliased with coefficients of orthogonal polynomials into the aliasing model, effectively improving the rank of the aliasing matrix and enabling one to separate multiple complex-valued images aliased together with only a single coil.

Appendix A

Since the separation process in Eq. (4) is not the inverse of the aliasing process in Eq. (1), the statistical properties of the separated images are not the same as those of the fully acquired images.

If the vector of observed and artificially aliased voxel values, y, has an expected value of

$$E[y] = \left(X_A \beta_R, (C\mu_R)^T, X_A \beta_I, (C\mu_I)^T \right)^T, \tag{A.1}$$

where $X_A\beta_R$ and $X_A\beta_I$ are the true mean real and imaginary aliased voxel values in the vector y, then the expected value of the voxels separated through the estimator in Eq. (4) will be

$$E\left[\hat{\beta}\right] = E\left[X^{-1}y\right] = X^{-1}E[y]. \tag{A.2}$$

Since the data vector, y, in Eq. (A.1) contains both the acquired aliased data and artificially aliased calibration data, the mean separated voxels in Eq. (A.2) are effectively a weighted average of the acquired and calibration measurements.

Appendix B Un-aliasing multiple FOV shifted acquisitions at once

The incorporation of calibration images into the SPECS model enables the number of aliased then separated slices using Eq. (4) to exceed the number of coils (in this case one) as the separating matrix is now of full rank. However, should the BOLD signal amplitude change in one or more of the voxels in y, the separation process may not be able to determine from which slice the increase originated. To properly separate aliased slices while preserving the origin of functional activations, it is necessary to observe multiple ways in which each voxel can be aliased with other voxels. One way to achieve this is to perform multiple acquisitions of aliased slices where the phase of each slice is strategically varied in a technique similar to the blipped-CAIPI model [30]. To illustrate this concept, consider $N_s = 4$ real-valued slices as in Fig. 1(a). The aliased images in Fig. 1(a) and (b) are merely two different linear combinations of the same voxel locations, represented by colored dots and spaced Δ apart in the PE dimension, within each of the $N_s = 4$ slices. Each of the aliased voxel measurements in the figure on the left results from a sum of the slices and can be separated using Eq. (4). Another possible acquisition would be to apply a FOV shift of $(j - 1)\Delta$ to the jth slice, where $\Delta = \text{FOV}/N_s$, resulting in the aliased image illustrated on the left of Fig. 1(b). Such a FOV shift can be performed on each
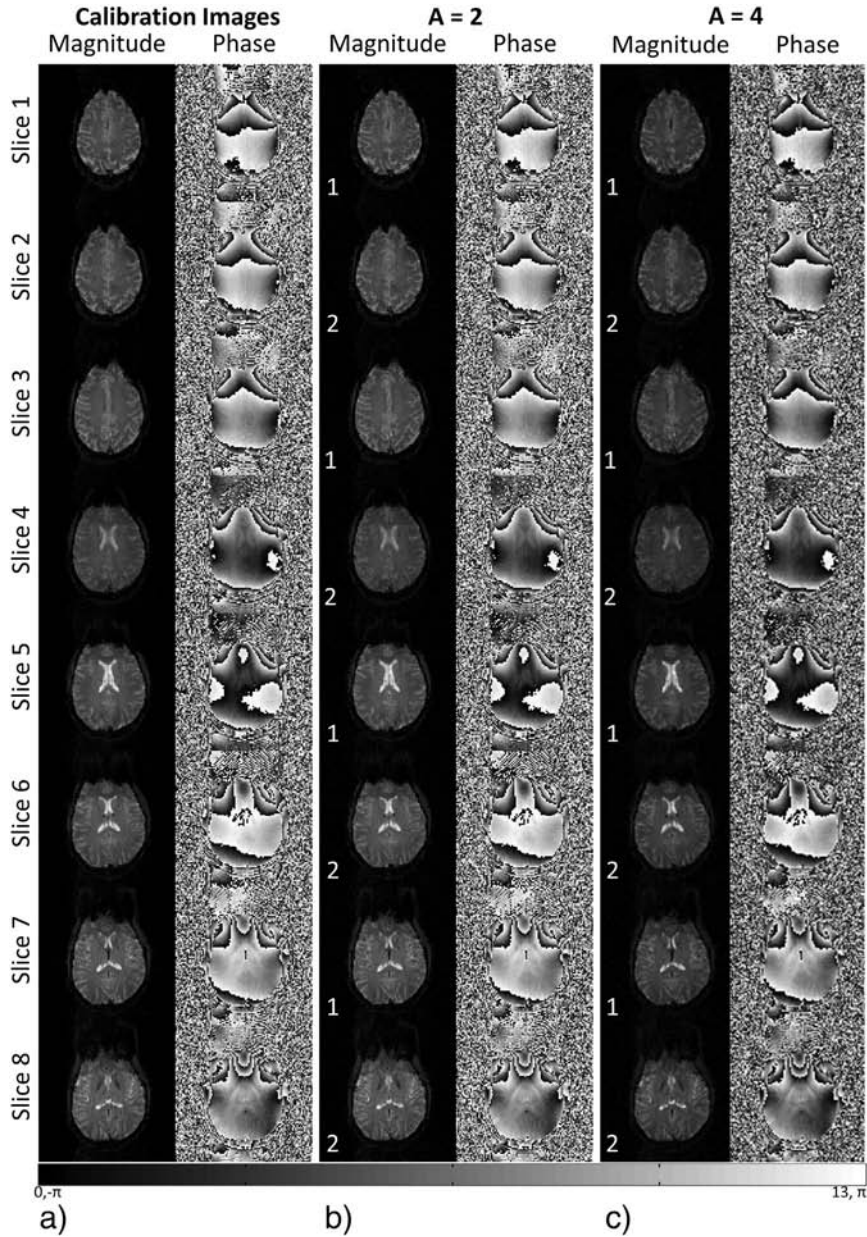
Fig. 7. For the first TR, the SPECS model separates the magnitude and phase images acquired by a single coil, as shown in Fig. 6, (a) with the mean of randomly selecting calibration slices into eight magnitude and phase images with no visual residual aliasing artifacts for (b) $A = 2$, and (c) $A = 4$. The white numbering scheme in (b) and (c) corresponds to the packet the slice was initially aliased into.

slice by appropriately applying slice select gradient blips concurrently with the phase encoding (PE) blips in EPI [30].

To incorporate the FOV shift in the SPECS model, both the real and imaginary components of the vector of true values, β, in Eq. (1) are expanded to have $N_S = 4$ sub-vectors (one for each slice) of the $N_S = 4$ voxel measurements equidistant spaced Δ apart within each slice. Since $N_S = 4$ voxel measurements are observed in each slice, the aliasing matrix, X_{A1}, corresponding to the first acquisition aliasing pattern in Fig. 1(a), becomes a row-wise concatenation of $N_S = 4$ identity matrices of size $N_S \times N_S = 4 \times 4$. When applied to the $N_S^2 \times 1$ vector β, the $N_S \times 1$ vector of aliased voxels is obtained by $a_1 = X_{A1}\beta + e_1$, where e_1 is measurement error. To obtain the vector of aliased voxels from the FOV shifted slices in Fig. 1(b), the identity matrices that comprise X_1 in Fig. 1(a) are individually permuted in X_{A2} to achieve a linear combination of the true fully

acquired voxel values in β. Combining the $N_{acq} = 2$ acquisitions in Fig. 1(a) and (b) creates a system of $N_S N_{acq} = 8$ equations with $N_S^2 = 16$ unknowns, rather than just one equation with $N_S = 4$ unknowns. To further improve the separation, additional acquisitions with the aliased slices shifted in unique patterns can be obtained. The SPECS model builds a system of $N_S N_{acq}$ equations and N_S^2 unknowns; increasing the N_{acq} sampling schemes improves the placement of functional activations in the correct separated slice, with an overall acceleration factor of $A = N_S / N_{acq}$.

Incorporating multiple acquisitions

As the aliased voxels in vectors a_1 and a_2 in Fig. 1 are derived from the $N_S = 4$ aliased voxels spaced Δ apart in each of the $N_S = 4$ slices, it is necessary for the slice separation matrix in Eq. (4) to be
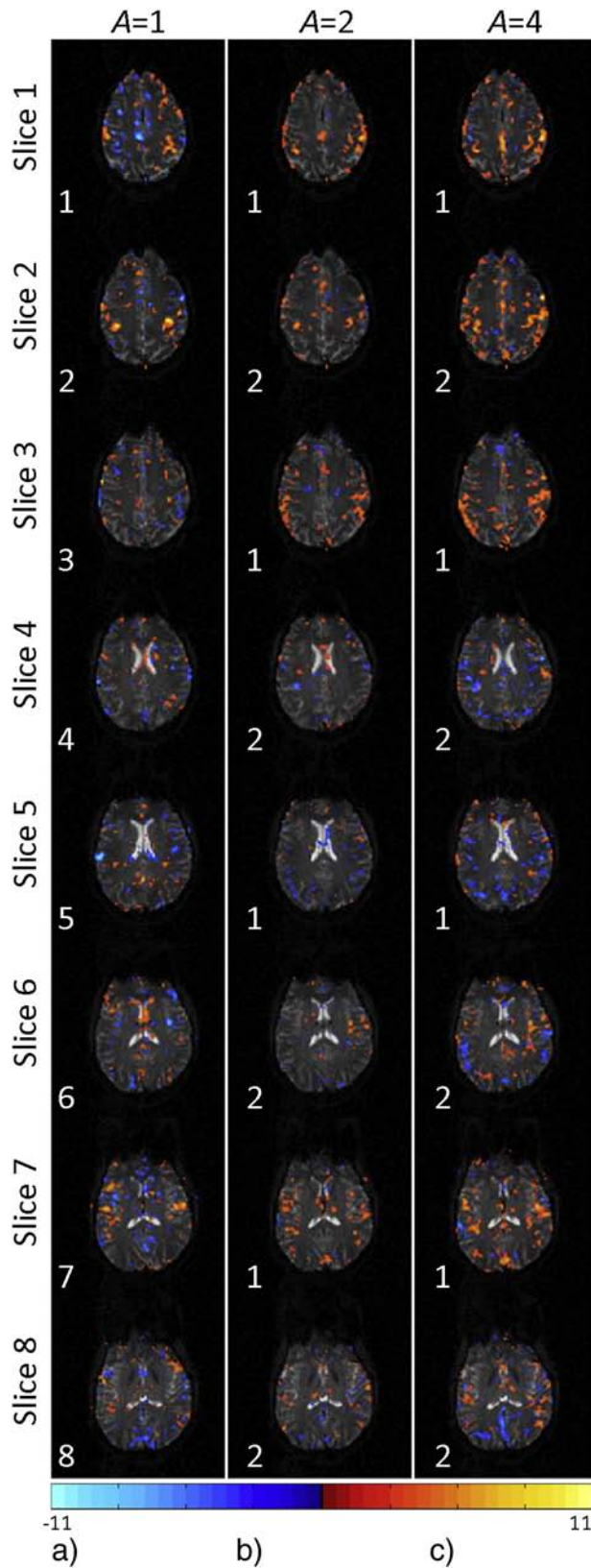
Fig. 8. With the experimental data simulation, fMRI activation statistics estimated with a complex-valued model in each voxel of each slice after separating 8 aliased slices with the SPECS model. Activation statistics are presented for data reconstructed from (a) eight acquisitions and eight packets, $A = 1$, (b) two acquisitions and two packets, $A = 2$, and (c) two acquisitions and one packet, $A = 4$. Pink squares indicate regions of true functional activity in slices. The white numbering scheme corresponds to the packet the slice was initially aliased into.

expanded to separating all $N_S^2 = 16$ voxel values in β at once. To generalize the model in Eq. (1) to having N_S slices aliased together in N_{acq} acquisitions, the vectors of aliased voxel values from each acquisition are stacked into a single complex-valued vector, $a = [a_1^T,...,a_{Nacq}^T]^T$, of length $N_S N_{acq}$. With the vector of true fully acquired voxel values, β, comprised of N_S sub-vectors of the N_S voxel measurements spaced Δ apart in the PE dimension within each slice, a combined aliasing matrix for the N_{acq} acquisitions, X, can be constructed through a column-wise concatenation of the aliasing matrices for each acquisition in Fig. 1 into a single matrix, $X_A = [X_{A1}^T,...,X_{ANacq}^T]^T$, of size $N_S N_{acq} \times N_S^2$. As shown in Fig. 1, the second dimension of the aliasing matrices is comprised of N_S permuted identity matrices that describe which row of the N_S values within a slice is incorporated in the aliased values in a. To incorporate the coefficients, C, from Eq. (3) into the model with $N_{acq} > 1$ acquisitions, we denote the block of N_S columns in X that correspond to slice j by X_j, and the jth column of the matrix C by C_j. The matrix, C, in Eq. (3) is replaced by $[X_1 \otimes C_1,...,X_{NS} \otimes C_{NS}]$ to create a new design matrix,

$$\begin{bmatrix} X_A \\ C \end{bmatrix} \rightarrow \begin{bmatrix} & X_{A1} & \\ & \vdots & \\ & X_{AN_{acq}} & \\ X_1 \otimes C_1, & \cdots & , X_{N_S} \otimes C_{N_S} \end{bmatrix}. \qquad (B.1)$$

The matrix in Eq. (B.1) combines the aliasing patterns of the observed measurements with the artificial aliasing patterns of the calibration measurements, resulting in an $N_S^2 N_{acq} \times N_S^2$ aliasing matrix. This over-determined system can therefore separate both the anatomical structure of the aliased images and functional activation and connectivity statistics. To complete the adaptation of Eq. (3) to simultaneously separate $N_{acq} > 1$ acquisitions, the vectors $\overline{\nu}_R$ and $\overline{\nu}_I$ are replaced by random calibration images that are shifted retrospectively to correspond with the shifted acquisitions before being artificially aliased with the matrix C.

References

[1] Sodickson DK, Manning WJ. Simultaneous acquisition of spatial harmonics (SMASH): fast imaging with radiofrequency coil arrays. Magn Reson Med 1997; 4:591–603.
[2] Pruessmann KP, Weiger M, Scheidegger MB, Boesiger P. SENSE: sensitivity encoding for fast MRI. Magn Reson Med 1999;42:952–62.
[3] Griswold MA, Jakob PM, Heidemann RM, Nittka M, Jellus V, Wang J, et al. Generalized autocalibrating partially parallel acquisitions (GRAPPA). Magn Reson Med 2002;47:1202–10.
[4] Muller S. Multifrequency selective RF pulses for multislice MR imaging. Magn Reson Med 1998;6:364–71.
[5] Souza SP, Szumowski J, Dumoulin CL, Plewes DP, Glover G. SIMA: simultaneous multislice acquisition of MR images by Hadamard-encoded excitation. J Comput Assist Tomogr 1988;12:1026–30.
[6] Larkman DJ, Hajnal JV, Herlihy AH, Coutts GA, Young IR, Ehnholm G. Use of multicoil arrays for separation of signal from multiple slices simultaneously excited. Magn Reson Imaging 2001;13:313–7.
[7] Breuer FA, Blaimer M, Heidemenn RM, Mueller MF, Griswold MA, Jakob PM. Controlled aliasing in parallel imaging results in higher acceleration (CAIPIRINHA) for multi-slice imaging. Magn Reson Med 2005;53:684–91.
[8] Moeller S, Auerbach E, van de Moortele PF, Adriany G, Ugurbil K. Functional MRI with 16-fold reduction using multibanded, multisite sampling. Proc Int Soc Magn Reson Med 2008;16:2366.
[9] Moeller S, Yacoub E, Auerbach E, Ohlman C, Ugurbil K. Unaliasing of multiband multislice EPI and GRE imaging with GRAPPA. Proc Int Soc Magn Reson Med 2009;17:1544.
[10] Jesmanowicz A, Nencka AS, Hyde JS. Two-fold phase encoded SENSE acceleration with a single-channel coil. Proc Int Soc Magn Reson Med 2011;19:2797.
[11] Jesmanowicz A, Li SJ, Hyde JS. Multi-slice two- and four-fold acceleration with single- and eight-channel coils, respectively. Proc Int Soc Magn Reson Med 2009; 17:1089.
[12] Moeller S, Yacoub E, Olman CA, Auerbach E, Strupp J, Harel N, et al. Multiband multislice GE-EPI at 7 tesla, with 16-fold acceleration using partial parallel imaging with application to high spatial and temporal whole-brain fMRI. Magn Reson Med 2010;63:1144–53.

[13] Feinberg DA, Moeller S, Smith SM, Auerbach E, Ramanna S, Glasser MF, et al. Multiplexed echo planar imaging for sub-second whole brain fMRI and fast diffusion imaging. PLoS One 2010;5:e15710.

[14] Jesmanowicz A, Nencka AS, Li SJ, Hyde JS. Two-axis acceleration of functional connectivity magnetic resonance imaging by parallel excitation of phase-tagged slices and half k-space acceleration. Brain Connectivity 2011;1:81–90.

[15] Moeller S, Xu J, Auerbach EJ, Yacoub E, Ugurbil K. Signal leakage (l-factor) as a measure of parallel imaging performance among simul- taneously multislice (SMS) excited and acquired signals. Proc Int Soc Magn Reson Med 2012:519.

[16] Setsompop K, Cauley SF, Bhat H, Polimeni J, Wald LL. Characterization and mitigation of signal leakage in simultaneous multi-slice (SMS) acquisition. Proc Int Soc Magn Reson Med 2013;21:3315.

[17] Cauley SF, Polimeni J, Bhat H, Wald LL, Setsompop K. Interslice leakage artifact reduction technique for simultaneous multislice acquisitions. Magn Reson Med 2014;72:93–102.

[18] Shefchik DS, Jesmanowicz A, Budde M, Nencka AS. Single-coil two-fold accelerated spin-echo phase-SENSE imaging of the rodent brain at 9.4 T. Proc Int Soc Magn Reson Med 2012;20:2229.

[19] Islam H, Glover G. Quadrature slice-encoding for reduced scan time. Proc Int Soc Magn Reson Med 2012;20:2285.

[20] Choli M, Breuer FA, Blaimer M. Simultaneous multi-slice imaging in combination with phase-sensitive parallel MRI. Proc Int Soc Magn Reson Med 2012;20:2228.

[21] Schneider JT, Blaimer M, Ullmann P. Tailoring the image background phase by spatially selective excitation for improved parallel imaging reconstruction performance. Proc Int Soc Magn Reson Med 2011;20:516.

[22] Lew C, Pineda AR, Clayton D, Spielman D, Chan F, Bammer R. SENSE phase-constrained magnitude reconstruction with iterative phase refinement. Magn Reson Med 2007;58:910–21.

[23] Blaimer M, Choli M, Jakob PM, Griswold MA, Breuer FA. Multiband phase constrained parallel MRI. Magn Reson Med 2013;69(4):974–80.

[24] Blaimer M, Gutberlet M, Kellman P, Bruer FA, Kostler H, Griswold MA. Virtual coil concept for improved parallel MRI employing conjugate symmetric signals. Magn Reson Med 2009;61:93–102.

[25] Rowe DB, Logan BR. A complex way to compute fMRI activation. NeuroImage 2004;23:1078–92.

[26] Rowe DB. Modeling both the magnitude and phase of complex-valued fMRI data. NeuroImage 2005;25:1310–24.

[27] Rowe DB. Magnitude and phase signal detection in complex-valued fMRI data. Magn Reson Med 2009;62:1356–7.

[28] Arja SK, Feng Z, Chen Z, Caprihan A, Kiehl KA, Adali T, et al. Changes in fMRI magnitude data and phase data observed in block-design and event-related tasks. NeuroImage 2010;49:3149–60.

[29] Rowe DB, Nencka AS, Jesmanowicz A, Hyde JS. Separation of two simultaneously encoded slices with a single coil. Proc Int Soc Magn Reson Med 2013;21:0123.

[30] Setsompop K, Gagoski BA, Polomeni JR, Witzel T, Wedeen VJ, Wald LL. Blipped-controlled aliasing in parallel imaging (blipped-CAIPI) for simultaneous multi-slice EPI with reduced g-factor penalty. Magn Reson Med 2012;67(5):1210–24.

[31] Harville DA. Matrix algebra from a statistician's perspective. Springer; 2008.

[32] Rowe DB, Nencka AS. Induced correlations in FMRI magnitude data from k-space preprocessing. Proc Int Soc Magn Reson Med 2009;17:1721.

[33] Karaman MM, Bruce IP, Rowe DB. Incorporating relaxivities to more accurately reconstruct MR images. Magn Reson Imaging 2015;33(4):85–96.

[34] Nencka AS, Hahn AD, Rowe DB. The use of three navigator echo in Cartesian EPI reconstruction reduces Nyquist ghosting. Proc Int Soc Magn Reson Med 2008;16:3032.

[35] Hahn A, Nencka AS, Rowe DB. Improving robustness and reliability of phase-sensitive fMRI analysis using temporal off resonance alignment of single-echo time series (TOAST). NeuroImage 2009;44:742–52.